applied sciences

MDPI

Article

Understanding Neutrophil Dynamics during COVID-19 Infection

Quiyana M. Murphy and Stanca M. Ciupe *

Department of Mathematics, Virginia Polytechnic Institute and State University, 225 Stanger Street, Blacksburg, VA 24060, USA
* Correspondence: stanca@vt.edu

Abstract: Infection with severe acute respiratory syndrome coronavirus 2 (SARS-CoV-2) results in varied clinical outcomes, with virus-induced chronic inflammation and tissue injury being associated with enhanced disease pathogenesis. To determine the role of tissue damage on immune populations recruitment and function, a mathematical model of innate immunity following SARS-CoV-2 infection has been proposed. The model was fitted to published longitudinal immune marker data from patients with mild and severe COVID-19 disease and key parameters were estimated for each clinical outcome. Analytical, bifurcation, and numerical investigations were conducted to determine the effect of parameters and initial conditions on long-term dynamics. The results were used to suggest changes needed to achieve immune resolution.

Keywords: mathematical modelling; neutrophils; COVID-19; SARS-CoV-2; inflammation; resolution; bifurcation analysis; sensitivity analysis

Citation: Murphy, Q.M.; Ciupe, S.M. Understanding Neutrophil Dynamics during COVID-19 Infection. *Appl. Sci.* **2023**, *13*, 2409. https://doi.org/10.3390/app13042409

Academic Editors: Yang Kuang, Kevin Flores and Erica Rutter

Received: 20 December 2022
Revised: 9 February 2023
Accepted: 9 February 2023
Published: 13 February 2023

1. Introduction

Infection with severe acute respiratory syndrome coronavirus 2 (SARS-CoV-2) results in varied individual coronavirus disease 2019 (COVID-19) outcomes ranging from asymptomatic to mild, severe, and fatal disease. The mechanisms responsible for the COVID-19 pathogenesis are not fully understood, but studies suggest that severe outcomes are driven by virus-induced reconfiguration of the innate immune system, which results in inflammation and tissue injury [1,2]. In severe and fatal SARS-CoV-2 infections, transcriptomic, epigenomic, and proteomic analyses revealed widespread dysfunction of peripheral innate immunity, aberrant interferon-related responses, recruitment of hyperactive macrophages and of functionally altered neutrophils, and the suppression of adaptive immunity (such as B-cells and T-cells function) [1,3,4]. Interferon-induced proinflammatory states stimulate uncontrolled complement activation and development of neutrophil extracellular traps (NETS), both of which induce overproduction and uncontrolled release of proinflammatory markers in a process known as cytokine storm [5,6], seen in other inflammatory diseases such as endotoxemia [7] and acute respiratory distress syndrome (ARDS)–complicated sepsis [8].

In general, inflammation can be viewed as a robust physiological process in which the body's innate immune system provides protection from adverse environmental factors. This process occurs while the immune system tries to resolve homeostatic perturbations initiated within the body (in autoimmune disease) or through external stimuli (bacteria, viral infections, injury, etc.) [9] with the goal of maintaining the structural integrity of tissues and organs [10]. Successful innate immune response is initiated within minutes and resolved within hours, with the affected tissues and immune populations returning to their homeostatic state [9]. Conversely, chronic inflammation results in continual recruitment to the tissue of neutrophils, macrophages, and inflammatory mediators whose activity persists for weeks, months or even years [9,11,12]. The persistent proinflammatory state induces further damage and recruitment of more inflammatory mediators. Several studies examined the differences in proinflammatory cellular and cytokine populations in patients

with mild and severe COVID-19 disease [13–16]. Data in [13] showed elevated levels of proinflammatory (IL-6, IL-2, and IFN-γ) and anti-inflammatory cytokines (IL-10), elevated levels of neutrophils and reduced levels of CD8 T-cells in patients with severe compared to those with mild COVID-19 disease. Similarly, [15] found elevated neutrophils levels, elevated IL-6 levels, and reduced levels of CD8 T-cells and CD4 T-cells in patients with severe or critical compared to those with moderate COVID-19. Elevated anti-inflammatory cytokines levels (IL-10) in severe disease was reported in [16], as well. Last, the neutrophil-to-CD8 T-cell ratio (N8R) has emerged as an early prognosis method for identifying severe COVID-19 disease [13], with high N8R ratio being indicative of severe outcomes [15,17,18].

While data exists for the magnitude of immune cells and proinflammatory mediators in different disease outcomes, little is known about the mechanistic interactions between these populations, and about the role that feedback, interpopulations effects and regulations play on overall disease outcomes. In this paper, we develop a mathematical model of interactions between neutrophils, macrophages, pro- and anti-inflammatory markers and CD8 T-cells and use it to tease out mechanisms responsible for COVID-19 pathogenesis. Previously, mathematical models have investigated human inflammation following physical injury [19–21], cancer [22,23], lung infections [10], rheumatoid arthritis [24,25], atherosclerosis [26], H. pylori [27], diabetes [28], and nonspecific pathogens [29–35]. Specifically, mathematical modeling of viral infections with pathogens such as influenza [36–40], hepatitis B [41–44], SARS-CoV [45,46], and SARS-CoV-2 [47–56] have investigated the role of immune responses in disease resolution or inflammation. Some of these studies highlighted the importance of cytokine production and neutrophil function in modulating disease pathogenesis.

In our study, we do not explicitly model the dynamics of SARS-CoV-2 infection, and instead only model the resulting inflammation. We consider interactions between neutrophils (active and apoptotic), macrophages, proinflammatory mediators, anti-inflammatory mediators and CD8 T-cells. We use the model to investigate the neutrophil responses to tissue damage caused by SARS-CoV-2 infection and to determine the mechanisms leading to resolution or inflammation. Moreover, we fit the model to longitudinal data from mild and severe COVID-19 infections to identify resolution or inflammation-specific parameters, such as the neutrophil-to-CD8 T-cell ratio. These results can inform interventions.

2. Materials and Methods

2.1. Mathematical Model

To determine the mechanistic interactions that lead to increased inflammation in severe COVID-19 infections, we develop a mathematical model of immune responses which extends on a previous model of nonspecific inflammation published in [30]. Briefly, we model the interaction between active and apoptotic neutrophils $n(t)$ and $a(t)$, macrophages $m(t)$, proinflammatory mediators $c(t)$, anti-inflammatory mediators $g(t)$, and CD8 T-cells $e(t)$ over time t, as follows. We assume that, following SARS-CoV-2 infection, epithelial tissue gets damaged according to function

$$f(t) = H(A\pi - t)\sin^2(pt), \tag{1}$$

where

$$H(A\pi - t) = \begin{cases} 1 & \text{if } t < A\pi/p \\ 0 & \text{if } t > A\pi/p, \end{cases} \tag{2}$$

as in [30]. Function Equation (1) accounts for A repeated cycles of tissue damage occurring every $2\pi/p$ days as a result of inflammatory processes triggered by SARS-CoV-2 infection (see Figure 1A for a schematic of a single $A = 1$ tissue damage cycle and Figure 1B for a schematic of four $A = 4$ tissue damage cycles for $p = 1$).

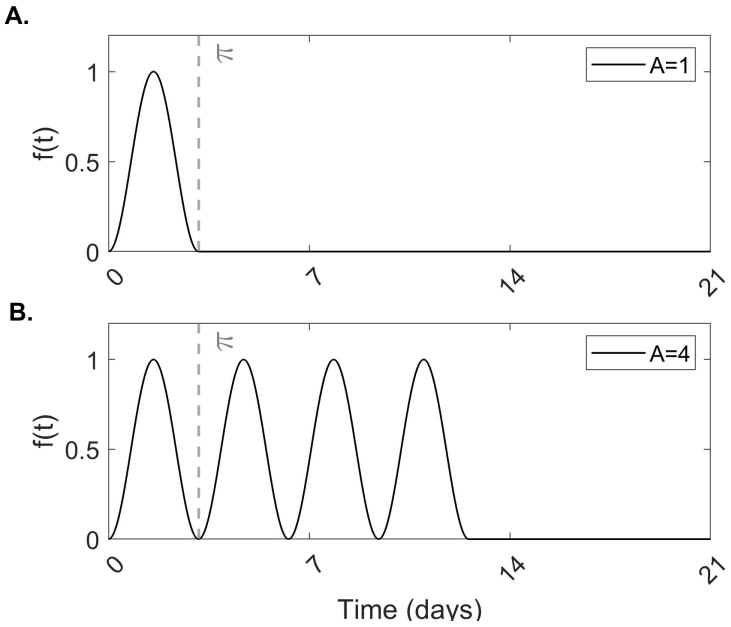

Figure 1. Tissue damage. Theoretical model of tissue damage $f(t)$ given by Equation (1) for (**A**) a single cycle of damage $A = 1$ and (**B**) four cycles of damage $A = 4$.

The physical damage to tissue results in release of cytokines that further enhance an inflammatory response. While there are a number of proinflammatory cytokines and mediators produced in response to tissue damage or viral infection (IL-1, IL-6, IL-8, TNF-α, among others [57]) we model them through a single proinflammatory population $c(t)$, which is produced at rate $\alpha f(t)$ and decays at per capita rate γ_c. This proinflammatory population recruits neutrophils and macrophages at the site of the inflammation. As in [30], we ignore neutrophil activation and differentiation and assume that activated neutrophils $n(t)$ are recruited at rate α_c and macrophages are recruited at rate α_m, respectively. Active neutrophils die and transform into apoptotic neutrophils $a(t)$ at rate $\nu g(t)$, proportional to regulatory factors $g(t)$ (in our model, the anti-inflammatory cytokine IL-10). Both active and apoptotic neutrophils contribute to increased production of proinflammatory mediators. Here, however, we only incorporate the contribution of apoptotic neutrophils, who undergo necrosis at rate γ_a, leading to damage of healthy tissue and hence further accumulation of proinflammatory factors $c(t)$ [11,58], as necrosis leads to release of toxic chemicals from internal granules [11,58–60]. We model this by adding a Hill-type production term with a Hill coefficient of two, $k_a \gamma_a a(t)^2/(a(t)^2 + \beta_a^2)$, into the proinflammatory population $c(t)$, which saturates at high $a(t)$ levels. Here, β_a is the concentration of neutrophils required for half-maximal release of proinflammatory mediators and k_a is the maximal level of proinflammatory population recruited after tissue damage.

We assume that macrophages $m(t)$ are recruited in response to proinflammatory mediators $c(t)$ at rate α_m, die at per capita rate γ_m, and contribute to the removal of apoptotic neutrophils through phagocytosis at rate ϕ. Recognition of apoptotic neutrophils by macrophages is thought to reprogram them to release anti-inflammatory signals, which recruit anti-inflammatory populations $g(t)$ at rate k_g. We assume that the anti-inflammatory population is present at low levels s_g/γ_g at the time of the infection, with s_g being the production rate and γ_g the per capita decay rate.

Lastly, we consider that the CD8 T-cell population $e(t)$ is present in the epithelium at base level s_e/γ_e, where s_e is the production and γ_e is the per capita death rate. Following viral infection, CD8 T-cells expand to become cytotoxic T-cells at rate α_e, proportional to the antigen-presenting cell concentration (in this case macrophages, $m(t)$). The expansion is suppressed in the presence of regulatory factors $g(t)$, in a density dependent manner with $1/\beta_e$ being the the concentration of regulatory factors where the effect is half-maximal.

A diagram of our model is given in Figure 2 and the model equations are

$$\begin{aligned}
\frac{dn}{dt} &= \alpha_c c - \nu g n, \\
\frac{da}{dt} &= \nu g n - \gamma_a a - \phi m a, \\
\frac{dm}{dt} &= \alpha_m c - \gamma_m m, \\
\frac{dc}{dt} &= \alpha f(t) + k_a \gamma_a \left(\frac{a^2}{\beta_a^2 + a^2} \right) - \gamma_c c, \\
\frac{dg}{dt} &= s_g + k_g \phi m a - \gamma_g g, \\
\frac{de}{dt} &= s_e + \frac{\alpha_e m}{1 + \beta_e g} - \gamma_e e,
\end{aligned} \tag{3}$$

subject to initial conditions $n(0) = n_0$, $a(0) = a_0$, $m(0) = m_0$, $c(0) = c_0$, $g(0) = g_0$, and $e(0) = e_0$.

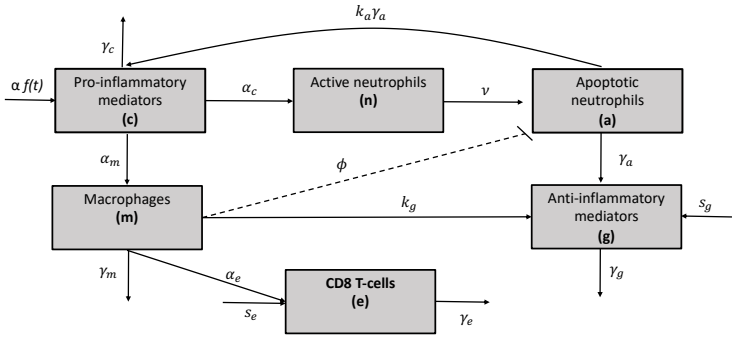

Figure 2. Network diagram for the mathematical model given in Equation (3).

2.2. Clinical Data

Longitudinal average and standard deviation values for total neutrophils, CD8 T-cells, and IL-10 were collected from 27 patients with mild and 13 patients with severe COVID-19 disease at days $t_j \in T = \{2, 5, 8, 11, 14, 17\}$ post hospitalization and previously published in [13]. Neutrophils and CD8 T-cells were measured in cells $\times 10^9$/L and IL-10 was measured in pg/mL (see Figure 3, red points and red error bars).

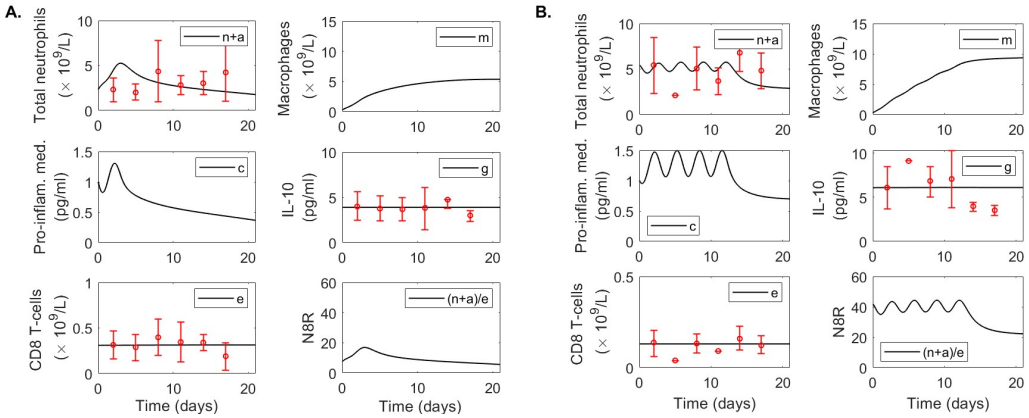

Figure 3. Data fitting results. Dynamics of variables defined by model Equation (3) over time for parameters in Tables 1 and 2 versus immunological data (red circles) in (**A**) mild and (**B**) severe COVID-19 infections. Time represents days post hospital admission. Error bars represent mean $\pm$ standard deviation where total neutrophil and CD8 T-cell data are given in $\times 10^9/L$ and IL-10 data in pg/mL as in [61].

2.3. Parameter Estimation

We use literature values for some of the parameters to reduce the model's degrees of freedom and allow for better estimation of the remaining parameters (see Table 1). The reported half-life of neutrophils is $t_{1/2,a}$ = 6–10 h [62]. We use a half-life of ten hours in our model, which corresponds to a decay rate $\gamma_a = ln(2)/t_{(1/2),a} = 1.66$ per day. Similarly, the reported half-life of alveolar macrophages is two weeks [63], corresponding to decay rate $\gamma_m = ln(2)/t_{(1/2),m} = 0.05$ per day. Nonactivated CD8 T-cell have a lifespan of 34 days [64], however, in the presence of antigen they expand into cytotoxic T-cells, who are short lived [65] with decay rate $\gamma_e = 0.5$ per day [44,66]. The IL-10 lifespan is 2.7–4.5 h [67]. Here, we assume a lifespan of 3.8 h, corresponding to a decay rate $\gamma_g = 6.2$ per day. Last, all proinflammatory mediators have a short half-life [68]. We use IL-6 in our model, whose half-life of 15 h [69], to obtain a decay rate $\gamma_c = 1.1$ per day. We assume that the initial neutrophils, CD8 T-cells and IL-10 are given by the hospitalization admission data, and we split the neutrophil data between active and apoptotic neutrophils $n(0) = a(0) = 0.5 \times (n + a)_{data}$ in both mild and severe cases. The initial macrophage number is $m(0) = 0.3 \times 10^9$ per L, corresponding to monocyte data upon hospital admission in [13]. Last, cytokine initial condition is set arbitrarily to $c_0 = 1 \times 10^9$ per L. We assume equilibrium conditions before hospitalization, hence the recruitment rates are $s_e = e(0)\gamma_e$ and $s_g = g(0)\gamma_g$. The initial tissue damage is set at $A = 1$ for the mild cases and $A = 4$ for the severe cases with $p = 1$ in both groups. All other parameters are chosen arbitrarily to be $\beta_e = \beta_a = 1$ cells, $\alpha_m = 0.7$ macrophages/(proinflammatory cells×day), $k_g = 15$ anti-inflammatory cells/ (apoptotic neutrophils) and $k_a = 0.6$ anti-inflammatory markers/(apoptotic neutrophils). A summary of fixed parameters is given in Table 1.

Table 1. Fixed parameter values and initial conditions.

Parameter	Description	Mild	Severe	Reference
γ_e	Decay rate of CD8 T-cells	0.5/day	0.5/day	[64]
γ_c	Decay rate of proinflammatory mediators	1.1/day	1.1/day	[69]
γ_g	Decay rate of $IL-10$	6.2/day	6.2/day	[70]
γ_m	Decay rate of alveolar macrophages	0.05/day	0.05/day	[63]
γ_a	Rate of necrosis of apoptotic neutrophils.	1.66/day	1.66/day	[62]
A	Cycles of tissue damage	1	4	–
α	Tissue damage magnitude	1	1	–
α_m	Macrophage recruitment rate	0.7	0.7	–
β_a	Neutrophils where proinflam. release is half-max.	1	1	–
β_e	Reg. cells where CD8 T-cell response is half-max.	1	1	–
s_g	T regulatory cells recruitment rate	$g(0)\gamma_g$	$g(0)\gamma_g$	–
s_e	CD8 T-cells recruitment rate	$e(0)\gamma_e$	$e(0)\gamma_e$	–
k_g	Anti-inflammatory production rate	15	15	–
n_0	Initial concentration of active neutrophils	0.5 × data	0.5 × data	[13]
a_0	Initial concentration of apoptotic neutrophils	0.5 × data	0.5 × data	[13]
m_0	Initial concentration macrophages	0.3×10^9/L	0.3×10^9/L	[13]
c_0	Initial concentration proinflammatory mediators	10^9/L	10^9/L	–
g_0	Initial concentration anti-inflammatory mediators	data	data	[13]
e_0	Initial concentration of CD8 T-cells	data	data	[13]
k_a	Max. level of proinflam. pop. recruited after damage	0.6	0.6	–

We assume time $t = 0$ in our model is the day of hospital admission and estimate the remaining parameters $\boldsymbol{\theta}_i = \{\alpha_e, \phi, \nu, \alpha_c\}$, by fitting the solution of model Equation (3) to IL-10, CD8 T-cells, and total neutrophil data given in [13] for mild and severe COVID-19 patients, where $i \in \{\text{mild}, \text{severe}\}$. Using the $fminsearch$ algorithm in Matlab, we minimize the objective function

$$J(\boldsymbol{\theta}_i) = \frac{1}{\max\limits_{t_j \in T}\{(n+a)_{data}(t_j)\}} \left(\sum_{t_j \in T} \left((n+a)(t_j, \boldsymbol{\theta}_i) - (n+a)_{data}(t_j) \right)^2 \right)^{1/2} + \frac{1}{\max\limits_{t_j \in T}\{e_{data}(t_j)\}} \left(\sum_{t_j \in T} \left(e(t_j, \boldsymbol{\theta}_i) - e_{data}(t_j) \right)^2 \right)^{1/2} + \frac{1}{\max\limits_{t_j \in T}\{g_{data}(t_j)\}} \left(\sum_{t_j \in T} \left(g(t_j, \boldsymbol{\theta}_i) - g_{data}(t_j) \right)^2 \right)^{1/2}, \quad (4)$$

where $n(t_j, \boldsymbol{\theta}_i)$, $a(t_j, \boldsymbol{\theta}_i)$, $g(t_j, \boldsymbol{\theta}_i)$, $e(t_j, \boldsymbol{\theta}_i)$ are the theoretical solutions of model Equation (3) at times t_j for parameters $\boldsymbol{\theta}_i$; $(n+a)_{data}(t_j)$, $g_{data}(t_j)$ and $e_{data}(t_j)$ are the neutrophil, IL-10 and CD8 T-cell data at times t_j as given in [13], and $t_j \in T = \{2, 5, 8, 11, 14, 17\}$ days post hospitalization. The best parameters estimates are given in Table 2.

Table 2. Best parameter estimates from fitting model Equation (3) to data from mild and severe COVID-19 cases.

Parameter	Description	Mild	Severe
α_e	CD8 T-cells expansion rate	1.2×10^{-2}	1.6×10^{-8}
ϕ	Rate at which macrophages engulf neutrophils	4.1×10^{-3}	3.3×10^{-4}
ν	Rate of neutrophil apoptosis	0.35	0.46
α_c	Neutrophil recruitment rate	3.44	4.28
ssq	Sum of squares	2.84	4.14

2.4. Semirelative Sensitivity Analysis

We conduct a formal semirelative sensitivity analysis of system Equation (3) with respect to the fitted parameters. Briefly, we let $X_\theta(t) = \frac{\partial X}{\partial \theta}(t)$ be the sensitivity curves of $X(t) = \{n(t), a(t), m(t), c(t), g(t), e(t)\}$ with respect to $\theta \in \{\alpha_c, \phi, \nu, \alpha_e\}$. Then $\theta X_\theta(t)$ are the semirelative sensitivity curves of $X(t)$ with respect to θ, which measure the change of $X(t)$ when parameter θ is doubled at time t. The corresponding sensitivity equations with respect to parameters θ are presented in Appendix A, Equations (A1)–(A4), and the corresponding semirelative curves are presented in Figures A3 and A4.

3. Results

Asymptotic Analysis Results

To determine the equilibrium solutions of model Equation (3), we assume that the initial tissue damage stimulus has been eliminated, and hence set $\alpha = 0$.

Proposition 1. *Model Equation (3) has a single equilibrium S_1 when*

$$\alpha_c < 2\beta_a\gamma_c \frac{1}{k_a} \sqrt{\frac{\alpha_m}{\gamma_m}\frac{\phi}{\gamma_c}k_a + 1} \quad (5)$$

and three equilibria S_1, S_2, and S_3 when

$$\alpha_c > 2\beta_a\gamma_c \frac{1}{k_a} \sqrt{\frac{\alpha_m}{\gamma_m}\frac{\phi}{\gamma_c}k_a + 1}. \quad (6)$$

Proof. We set $\frac{d\bar{X}}{dt} = 0$ for $\bar{X} = \{\bar{n}, \bar{m}, \bar{c}, \bar{g}, \bar{e}\}$ in Equation (3) and solve for components of vector $\bar{X}$ in terms of $\bar{a}$. This yields the following expressions

$$\begin{aligned}
\bar{n} &= \frac{\bar{a}^3(\gamma_a\gamma_g\alpha_m\phi k_a) + \bar{a}\left(\bar{a}^2+\beta_a^2\right)\gamma_c\gamma_m\gamma_g\gamma_a}{\bar{a}^3(\gamma_a\alpha_m\nu k_g\phi k_a) + (\bar{a}^2+\beta_a^2)\gamma_c\gamma_m\nu s_g},\\
\bar{m} &= \frac{\alpha_m}{\gamma_m}\frac{\gamma_a k_a}{\gamma_c}\frac{\bar{a}^2}{(\bar{a}^2+\beta_a^2)},\\
\bar{c} &= \frac{\gamma_a k_a}{\gamma_c}\frac{\bar{a}^2}{(\bar{a}^2+\beta_a^2)},\\
\bar{g} &= \frac{s_g}{\gamma_g} + \frac{\alpha_m}{\gamma_m}\frac{\gamma_a k_g\phi k_a}{\gamma_c\gamma_g}\frac{\bar{a}^3}{(\bar{a}^2+\beta_a^2)},\\
\bar{e} &= \frac{s_e}{\gamma_e} + \frac{\bar{a}^2(\alpha_e\alpha_m\gamma_a\gamma_g k_a)}{\bar{a}^3(\gamma_e\alpha_m\beta_e\gamma_a k_g\phi k_a) + (\bar{a}^2+\beta_a^2)\gamma_e\gamma_c\gamma_m(s_g\beta_e+\gamma_g)}.
\end{aligned} \tag{7}$$

Next, we solve for $\bar{a}$ by substituting $\bar{c}$ and $\bar{m}$ into

$$\frac{d\bar{a}}{dt} = \alpha_c\bar{c} - (\gamma_a\bar{a} + \phi\bar{m}\bar{a}) = 0.$$

Simplifying yields

$$0 = \bar{a}\left[\bar{a}^2(\gamma_a\gamma_c\gamma_m + k_a\phi\alpha_m\gamma_a) - \bar{a}(\alpha_c k_a\gamma_a\gamma_m) + \beta_a^2\gamma_a\gamma_c\gamma_m\right], \tag{8}$$

which has one solution

$$\bar{a}_1 = 0, \tag{9}$$

when

$$\alpha_c < 2\beta_a\gamma_c\frac{1}{k_a}\sqrt{\frac{\alpha_m}{\gamma_m}\frac{\phi}{\gamma_c}k_a + 1},$$

and three solutions

$$\begin{aligned}
\bar{a}_1 &= 0,\\
\bar{a}_{2,3} &= \frac{\alpha_c\gamma_m k_a \pm \sqrt{\gamma_m}\sqrt{\alpha_c^2\gamma_m k_a^2 - 4\beta_a^2\gamma_c^2\gamma_m - 4\alpha_m\beta_a^2\gamma_c\phi k_a}}{2(\gamma_c\gamma_m + \alpha_m\phi k_a)},
\end{aligned} \tag{10}$$

when

$$\alpha_c > 2\beta_a\gamma_c\frac{1}{k_a}\sqrt{\frac{\alpha_m}{\gamma_m}\frac{\phi}{\gamma_c}k_a + 1}. \tag{11}$$

Since $\{\bar{n}, \bar{m}, \bar{c}, \bar{g}, \bar{e}\}$ are positive when $\bar{a}$ is positive, we obtain that a single equilibrium solution called *no-inflammation* equilibrium exists when condition Equation (5) holds,

$$S_1 = (0, 0, 0, 0, \frac{s_g}{\gamma_g}, \frac{s_e}{\gamma_e}).$$

Conversely, three equilibria solutions exist when condition Equation (6) holds. They are S_1 (as before) and

$$S_{2,3} = (\bar{n}, \bar{m}, \bar{a}, \bar{c}, \bar{g}, \bar{e})_{2,3}$$

given by Equations (7) and (10) and called *chronic inflammation* equilibria. This concludes our proof. □

Proposition 2. *The no-inflammation equilibrium S_1 exists and is locally asymptotically stable for all parameters.*

Proof. The Jacobian associated with system Equation (3) at equilibrium point $S = (\bar{n}, \bar{a}, \bar{m}, \bar{c}, \bar{g}, \bar{e})$ is

$$J(S) = \begin{bmatrix} -\nu\bar{g} & 0 & 0 & \alpha_c & -\nu\bar{n} & 0 \\ \nu\bar{g} & -\gamma_a - \phi\bar{m} & -\phi\bar{a} & 0 & \nu\bar{n} & 0 \\ 0 & 0 & -\gamma_m & \alpha_m & 0 & 0 \\ 0 & 2\gamma_a k_a \beta_a^2 \dfrac{\bar{a}}{(\bar{a}^2+\beta_a^2)^2} & 0 & -\gamma_c & 0 & 0 \\ 0 & k_g\phi\bar{m} & k_g\phi\bar{a} & 0 & -\gamma_g & 0 \\ 0 & 0 & \dfrac{\alpha_e}{1+\beta_e\bar{g}} & 0 & -\dfrac{\alpha_e\beta_e\bar{m}}{(1+\beta_e\bar{g})^2} & -\gamma_e \end{bmatrix}. \quad (12)$$

The corresponding characteristic equation at the no-inflammation equilibrium point

$$S_1 = (\bar{n}_1, \bar{a}_1, \bar{m}_1, \bar{c}_1, \bar{g}_1, \bar{e}_1) = (0, 0, 0, 0, s_g/\gamma_g, s_e/\gamma_e)$$

is

$$\det(J(S_1) - \lambda I_6) = (\lambda+\gamma_e)(\lambda+\gamma_g)(\lambda+\gamma_c)(\lambda+\gamma_m)(\lambda+\gamma_a)(\lambda+\frac{s_g\nu}{\gamma_g}) = 0,$$

with eigenvalues $\lambda_1 = -\gamma_a < 0$, $\lambda_2 = -\gamma_c < 0$, $\lambda_3 = -\gamma_e < 0$, $\lambda_4 = -\gamma_g < 0$, $\lambda_5 = -\gamma_m < 0$, and $\lambda_6 = -\dfrac{s_g\nu}{\gamma_g} < 0$. Therefore, the no-inflammation equilibrium is always locally asymptotically stable. □

Proposition 3. *One of the chronic inflamation equolibria is always unstable and the other is locally asymptotocally stable when condition (6) holds.*

Proof. The characteristic equation for the chronic-inflammation equilibria S_i, $i \in \{2, 3\}$ is

$$\det(J(S_i) - \lambda I_6) = (\lambda+\gamma_e)(\lambda^5 + A_1\lambda^4 + A_2\lambda^3 + A_3\lambda^2 + A_4\lambda + A_5) = 0,$$

where

$$\begin{aligned}
A_1 &= \bar{g}_i\nu + \bar{m}_i\phi + \gamma_a + \gamma_c + \gamma_g + \gamma_m, \\
A_2 &= \bar{m}_i\nu\phi(\bar{g}_i - k_g\bar{n}_i) + \bar{g}_i(\gamma_a+\gamma_c+\gamma_g+\gamma_m)\nu + (\bar{m}_i\phi+\gamma_a)(\gamma_c+\gamma_g+\gamma_m) + \gamma_c(\gamma_g+\gamma_m) + \gamma_g\gamma_m, \\
A_3 &= \bar{m}_i\nu\phi(\bar{g}_i - k_g\bar{n}_i) + \bar{g}_i(\gamma_a+\gamma_c+\gamma_g+\gamma_m)\nu + \bar{m}_i\phi(\gamma_c+\gamma_g+\gamma_m) + \gamma_a(\gamma_c+\gamma_g+\gamma_m) \\
&\quad + \gamma_c(\gamma_g+\gamma_m) + \gamma_g\gamma_m, \\
A_4 &= \bar{g}_i\bar{m}_i(\gamma_c\gamma_g + \gamma_c\gamma_m + \gamma_g\gamma_m)\nu\phi + \bar{m}_i\gamma_c\gamma_m(\gamma_g\phi - k_g\nu\phi\bar{n}_i) + \bar{g}_i(\gamma_a\gamma_c(\gamma_g+\gamma_m) + \gamma_m\gamma_g(\gamma_a+\gamma_c)\nu\phi \\
&\quad + \gamma_a\gamma_c\gamma_g\gamma_m - \frac{\beta_a^2}{(\bar{a}_i+\beta_a^2)^2}(2\alpha_m\gamma_a(\bar{g}_i\nu - k_g\bar{n}_i\nu + \gamma_g)\phi + \bar{g}_i\gamma_c\gamma_g\bar{m}_i\nu\phi + \bar{g}_i(\gamma_c\gamma_m + \gamma_g\gamma_m)\nu\phi \\
&\quad - \gamma_c\gamma_m k_g\bar{m}_i\bar{n}_i\nu\phi + \bar{g}_i(\gamma_a\gamma_c\gamma_g + \gamma_a\gamma_c\gamma_m + \gamma_a\gamma_g\gamma_m + \gamma_c\gamma_g\gamma_m)\nu + \bar{m}_i\gamma_c\gamma_g\gamma_m\phi + \gamma_a\gamma_c\gamma_g\gamma_m), \\
A_5 &= \bar{g}_i\gamma_c\gamma_g\gamma_m\nu(\bar{m}_i\phi + \gamma_a) + 2\frac{\bar{a}_i\bar{g}_i\beta_a^2}{(\beta_a^2+\bar{a}_i^2)^2}(\bar{a}_i\alpha_m\gamma_g\phi - \alpha_c)\gamma_a\nu.
\end{aligned} \quad (13)$$

By Routh-Hurwitz conditions, we have eigenvalues with negative real parts (and hence local asymptotoc stability for $S_{2,3}$) if and only if the Hurwitz matrices H_i for $i = \{1, \ldots, 5\}$

$$
\begin{aligned}
H_1 &= \begin{bmatrix} A_1 \end{bmatrix}, \\
H_2 &= \begin{bmatrix} A_1 & A_3 \\ 1 & A_2 \end{bmatrix}, \\
H_3 &= \begin{bmatrix} A_1 & A_3 & A_5 \\ 1 & A_2 & A_4 \\ 0 & A_1 & A_3 \end{bmatrix}, \\
H_4 &= \begin{bmatrix} A_1 & A_3 & A_5 & 0 \\ 1 & A_2 & A_4 & 0 \\ 0 & A_1 & A_3 & A_5 \\ 0 & 1 & A_2 & A_4 \end{bmatrix}, \\
H_5 &= \begin{bmatrix} A_1 & A_3 & A_5 & 0 & 0 \\ 1 & A_2 & A_4 & 0 & 0 \\ 0 & A_1 & A_3 & A_5 & 0 \\ 0 & 1 & A_2 & A_4 & 0 \\ 0 & 0 & A_1 & A_3 & A_5 \end{bmatrix},
\end{aligned}
\tag{14}
$$

have positive determinants. This simplifies to $\Delta_1 = \det(H_1) = A_1 > 0$ which is always true, $\Delta_2 = \det(H_2) = A_1A_2 - A_3 > 0$, $\Delta_3 = \det(H_3) = A_3\Delta_2 - A_1(A_1A_4 - A_5) > 0$, and $\Delta_4 = \det(H_4) = A_4\Delta_3 - A_5(A_1A_2^2 - A_1A_4 - A_2A_3 + A_5) > 0$, and $\Delta_5 = \det(H_5) = A_5\Delta_4 > 0$ which happens for $\Delta_4 > 0$ and

$$
\alpha_c > \bar{a}_i\alpha_m\gamma_g\phi + \frac{(\beta_a^2 + \bar{a}_i^2)^2}{2\bar{a}_i^2(\bar{m}_i\phi + \gamma_a)\beta_a^2}\frac{\gamma_c\gamma_m\nu}{\alpha_m\phi}. \tag{15}
$$

Solving Equation (14) is cumbersome, so we will present numerical results for the stability of the chronic-inflammation states S_2 and S_3 from here on. □

4. Numerical Results

4.1. Parameter Variability Between Disease Outcomes

Using the data fitting approach described above, we obtained good fits of model Equation (3) to data from patients with mild disease (Figure 3A) and severe disease (Figure 3B). In Table 2, we present the parameter estimates corresponding to the best fits. The neutrophil apoptosis rate ν is higher in severe compared to mild cases, $\nu = 0.46/(\text{anti-inflam} \times \text{day})$ compared to $\nu = 0.35/(\text{anti-inflam} \times \text{day})$, which implies that the change in neutrophil phenotype is disease status dependent. Similarly, neutrophil recruitment rate α_c is larger in the severe compared to the mild cases, $\alpha_c = 4.28$ neutrophils/(proinflamm $\times$ day) compared to $\alpha_c = 3.44$ neutrophils/(pro-inflamm $\times$ day), respectively. By contrast, the rate at which macrophages remove apoptotic neutrophils ϕ is lower in the severe compared to the mild cases, $\phi = 3.3 \times 10^{-4}$ neutrophils/(macrophage$\times$ day) compared to $\phi = 4.1 \times 10^{-3}$ neutrophils/(macrophage $\times$ day), respectively. The biggest difference between the two groups, however, is in the recruitment of CD8 T-cells, with the severe patients' recruitment rate being six order of magnitude lower than the mild patients' recruitment rate, $\alpha_e = 1.6 \times 10^{-8}$ CD8 T-cells/(macrophage$\times$ day) compared to $\alpha_e = 1.2 \times 10^{-2}$ CD8 T-cells/(macrophage $\times$ day), respectively. We observe different long-term dynamics between mild and severe cases for total neutrophils $n(t) + a(t)$, proinflammatory mediator $c(t)$ and macrophages $m(t)$, with these populations asymptotically reaching extinction (no-inflammation equilibrium state) in the mild case and persisting at positive levels (chronic-equilibrium state) for severe case (see Figure 4). By contrast, data fitting predicts that the equilibria values for CD8 T-cell and IL-10 populations settle close to the populations' initial conditions (which correspond to the first mild and severe CD8 T-cell and IL-10 clinical data points, respectively). Hence, as seen in the data, the CD8 T-cell equilibrium value is 2.4-times higher in mild patients, $\bar{e}_m = 0.31 \times 10^9$/L, compared to severe patients, $\bar{e}_s = 0.13 \times 10^9$/L. Conversely, as seen in the data, the IL-10 equilibrium value is 36% lower in mild patients $\bar{g}_m = 3.9$ pg/mL compared to the severe patients, $\bar{g}_s = 6.1$ pg/mL (see Figure 4).

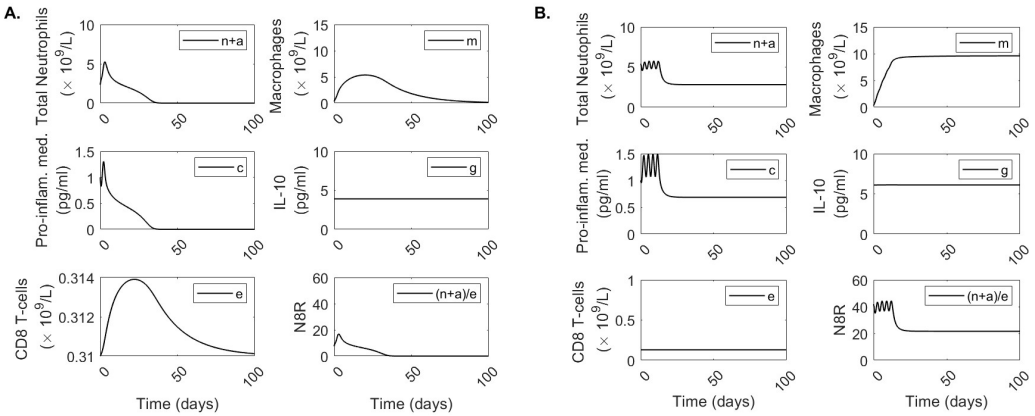

Figure 4. Long-term dynamics. Dynamics of model Equation (3) over 100 days for parameters for (**A**) mild and (**B**) severe COVID-19 infections.

4.2. Bifurcation Analysis

The stability analysis shows bistable behavior between the no-inflammation and chronic-inflammation states when conditions Equations (11) and (14) hold. To determine the parameter space where bistability exists and its relationship with the estimated mild and severe parameters we constructed α_c and ϕ bifurcation diagrams. In both diagrams, we start with parameters and initial conditions estimated from severe cases and vary α_c and ϕ, respectively. Figure 5 shows that, for low neutrophil recruitment rates $\alpha_c < 3.67$, only the no-inflammation equilibrium exists and is stable. This range includes the mild case $\alpha_c = 3.44$ value (see Figure 5, green line). For larger neutrophil recruitment rates $\alpha_c > 3.67$, we obtain bistability of the no-inflammation and chronic-inflammation equilibria. The range includes the severe case $\alpha_c = 4.28$ value (see Figure 5, red line). The dynamical transition happens at the bifurcation point $\alpha_c^{critical} = 3.67$. These results suggest that when starting with the severe outcome setup, we only need to lower neutrophil recruitment rates to speedup the resolution of inflammation, independently of the other biological processes.

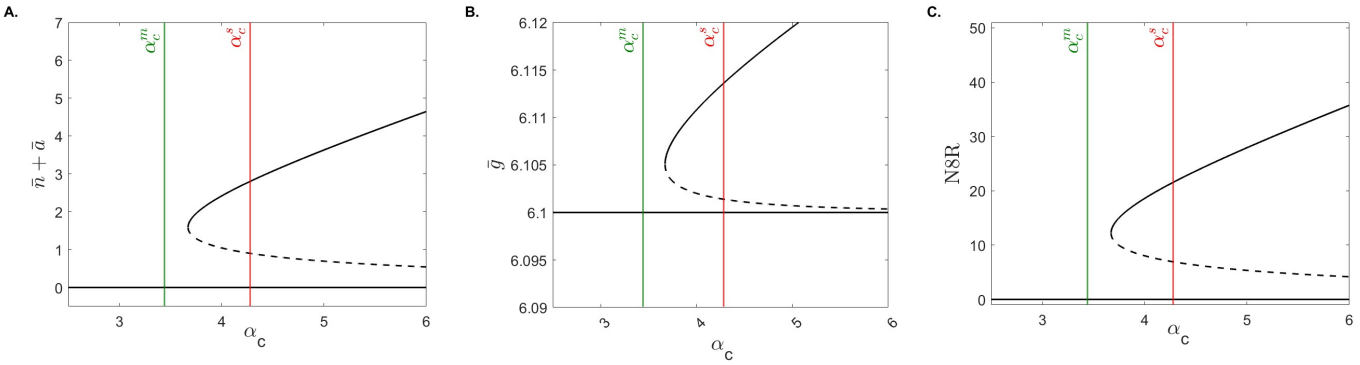

Figure 5. The α_c bifurcation diagram. Stable (solid black curves) and unstable (dashed black curves) population equilibria for varied α_c for (**A**) total neutrophils $\bar{n}+\bar{a}$, (**B**) IL-10 $\bar{g}$, and (**C**) N8R $(\bar{n}+\bar{a})/\bar{e}$. The green and red lines are the α_c values from the mild and severe cases, α_c^m and α_c^s.

Conversely, Figure 6 shows that, for low macrophage phagocytosis rates $\phi < 0.047$, we obtain bistability of the no-inflammation and chronic-inflammation equilibria. For higher macrophage phagocytosis rates $\phi > 0.047$ we obtain that only the no-inflammation equilibrium exists and is stable. The transition happens at the bifurcation point $\phi^{critical} = 0.047$. Unlike the α_c bifurcation diagram, however, we note that both the mild and severe ϕ values are in the bistable region (see Figure 6, green and red lines) suggesting that the resolution of inflammation seen in the mild case is dependent on other parameters and/or initial conditions.

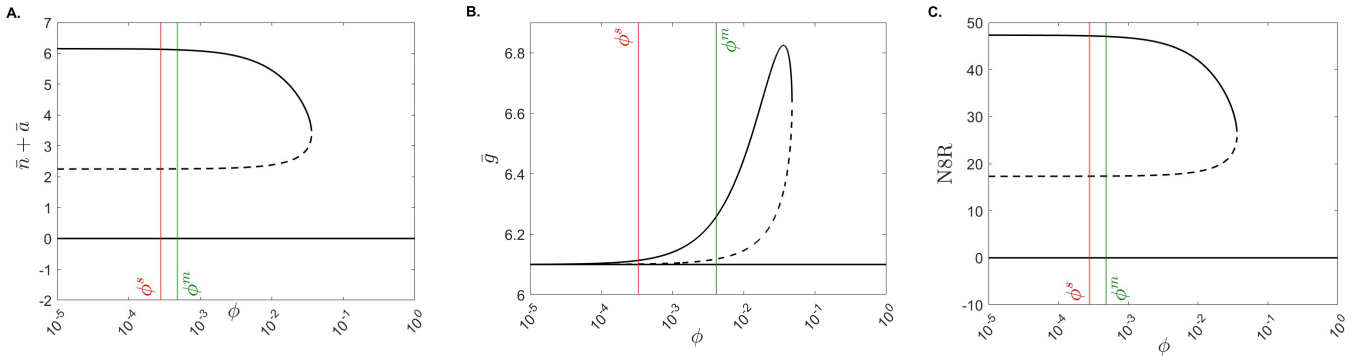

Figure 6. The ϕ bifurcation diagram. Stable (solid black curves) and unstable (dashed black curves) population equilibria for varied ϕ for (**A**) total neutrophils $\bar{n}+\bar{a}$, (**B**) IL-10 $\bar{g}$, and (**C**) N8R $(\bar{n}+\bar{a})/\bar{e}$. The green and red lines are the ϕ values from the mild and severe cases, ϕ^m and ϕ^s.

4.3. Basin of Attraction

We next determine the basins of attraction for the no-inflammation and chronic-inflammation equilibrium states. For simplicity, we assumed that all parameters and initial conditions are given in Tables 1 and 2 (severe case), fixed $\alpha_c = \alpha_c^{critical} = 3.67$ and varied activated neutrophils and anti-inflammatory mediators initial conditions $(g_0, n_0) \in \{0.1 < g_0 < 1, 0 \leq n_0 \leq 20\}$. Under these assumptions, we find a large basin of attraction for the chronic-inflammation equilibrium state $S_3 = (\bar{n}_3, \bar{a}_3, \bar{m}_3, \bar{c}_3, \bar{g}_3, \bar{e}_3)$ where $n_0 > 2$ and $g_0 > 1.2$ and a small basin of attraction for the no-inflammation equilibrium state $S_1 = (\bar{n}_1, \bar{a}_1, \bar{m}_1, \bar{c}_1, \bar{g}_1, \bar{e}_1) = (0, 0, 0, 0, s_g/\gamma_g, s_e/\gamma_e)$ for small g_0 and n_0 values (see Figure 7A). This means that for low initial anti-inflammatory markers, the inflammation is resolved when few active neutrophils are recruited and inflammation persists otherwise. We further investigate how the basin of attraction for the no-inflammation equilibrium S_1 changes when we fix $g_0 = 0.1$ pg/mL and vary both the initial activated neutrophils number $0 \leq n_0 \leq 20$ and the macrophage phagocytosis rate $10^{-5} < \phi < 0.1$. We find that for high macrophage phagocytosis rate ϕ, the no-inflammation equilibrum state is an attracting set for all $0 \leq n_0 \leq 20$, while for low macrophage phagocytosis rate ϕ the no-inflammation equilibrium state is an attracting set only when the initial activated neutrophil level is small (see Figure 7B).

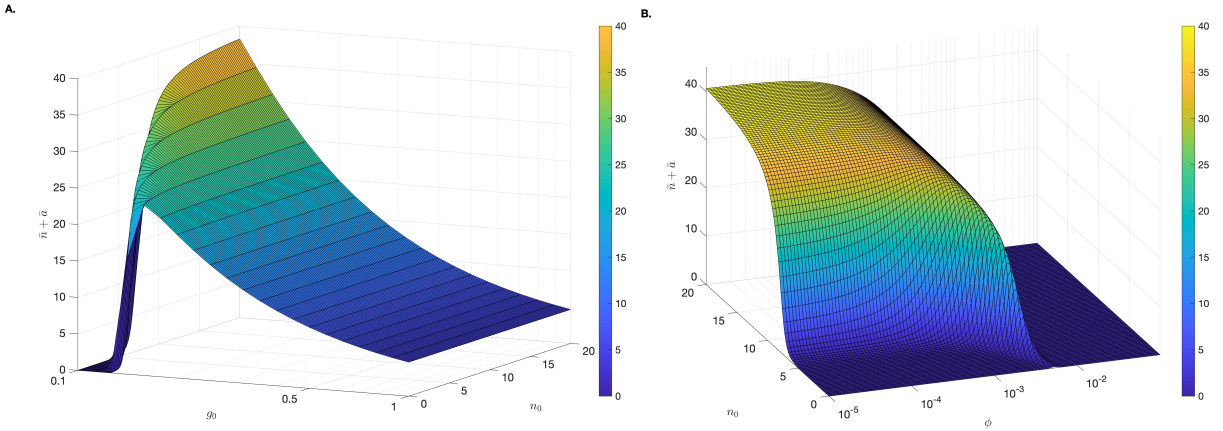

Figure 7. Basin of attraction. Attracting asymptotic solutions $\bar{n}+\bar{a}$ for (**A**) different initial condition n_0 and g_0 (**B**) $g_0 = 0.1$, different initial condition n_0 and changing parameter ϕ. We fix $\alpha_c = 3.67$ neutrophils/(macrophage $\times$ day) and all other parameters are as in Tables 1 and 2 (severe case). Note that g_0 and ϕ are plotted on log scale.

4.4. The Role of Tissue Damage on Immune Resolution

All the stability results presented above assumed that the tissue damage function can be ignored by setting $\alpha = 0$. To determine how relaxing this condition affects dynamics we investigate the short- and long-term behavior of total neutrophils $n(t) + a(t)$ and proinflammatory cytokines $c(t)$ when we vary (i) the frequency of oscillations $p \in \{1, 10, 0.1\}$, (ii) the number of tissue damage cycles $A \in \{1, 10, 0.1\}$, and (iii) the magnitude effect that tissue damage has on the proinflammatory cytokine recruitment rate $\alpha \in \{1, 10, 0.1\}$. We start with parameters and initial conditions in Tables 1 and 2 (severe case), and $\phi = 0.046 < \phi^{critical}$, which results in resolution of inflammation for the baseline assumptions $p = A = \alpha = 1$. We then increase or decrease one of the tissue damage parameters $\{p, A, \alpha\}$ while leaving the other two unchanged. We find that the frequency of oscillations p has no significant effect of the short- and long-term $n(t) + a(t)$ and $c(t)$ dynamics (see Figure 8A). The number of tissue damage cycles A, however, has a significant effect on the length of inflammation, with many rounds of tissue damage resulting in prolonged inflammation which persists for longer than 100 days for $A = 10$ (see Figure 8B, red curves) and is resolved in 50 days for $A = 1$ (see Figure 8B, black curves). The long-term dynamics, however, do not change with the no-inflammation equilibrium state being reached regardless of A. Last, the magnitude of tissue damage, α, has a transient effect of both $n(t) + a(t)$ and $c(t)$ dynamics. In particular, a large $\alpha = 10$ leads to a large transient increase in both total neutrophils and proinflammatory markers over the first 20 days (see Figure 8C, red curves), while a small $\alpha = 0.1$ has a low overall effect (see Figure 8C, blue curves). Interestingly, the transient effect is prolonged for low α and decays faster for high α.

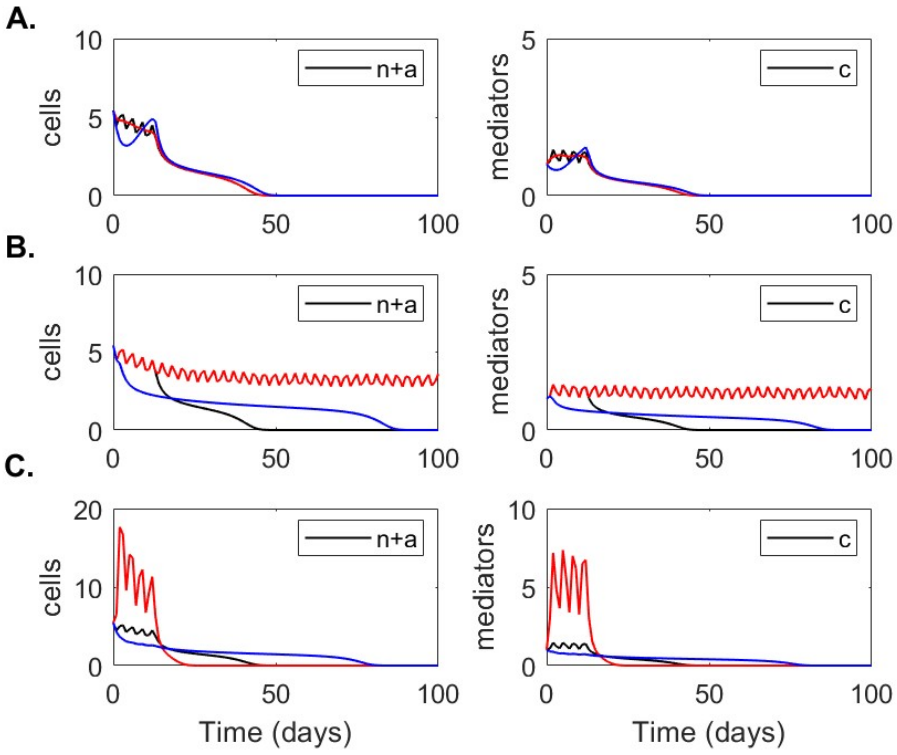

Figure 8. Dynamics for different $f(t)$ functions. Dynamics of model Equation (3) over 100 days for (**A**) $p = 0.1$ (blue line), $p = 1$ (black line), $p = 10$ (red line); (**B**) $A = 0.1$ (blue line), $A = 1$ (black line), $A = 10$ (red line); and (**C**) $\alpha = 0.1$ (blue line), $\alpha = 1$ (black line), $\alpha = 10$ (red line). The other parameters are given in Table 1 and Table 2 (severe case) and $\phi = 0.047$.

4.5. Neutrophils-to-CD8 T-Cell Ratio

One marker commonly used for deciding disease severity is the nuetrophils-to-CD8 T-cell ratio, N8R [13,15]. In the context of COVID-19 pathogenesis, the reported N8R median for mild cases is 9.0 (ranges 5.9–14.0) in [15], while the reported N8R median for severe cases is 15.7 (IQR: 9.7–24.6) in [15] and 44.1 (range 39.8–49.4) in [13]. In our model, the N8R ratio at time t is given by

$$N8R = \frac{n(t) + a(t)}{e(t)}. \tag{16}$$

For mild cases, nuetrophils-to-CD8 T-cell ratio peaks 3.25 days after hospital admission to $N8R = 13.1$ and decays to zero in the long-run. By contrast, for severe cases, the nuetrophils-to-CD8 T-cell ratio starts at $N8R = 41$ at the time of hospital admission and settles at $N8R = 38$ in the long-run.

5. Discussion

In this paper, we developed a mathematical model of innate immunity following SARS-CoV-2 infection that describes neutrophils recruitment into the lungs following epithelial tissue damage and investigates their role in inducing disease resolution or in enhancing disease pathogenesis. We studied the model analytically and numerically and determined that it exhibits monostable and bistable kinetics, where the monstable state corresponds to immune resolution and the bistable state corresponds to tradeoff between immune resolution and chronic-inflammation. We fitted the model to immune marker data from patients with mild and severe COVID-19 disease published in [61]. We estimated several key parameters for each clinical outcome group and determined the immune-specific differences between the groups. We examined the effect on the systems' long-term behavior of parameters and initial conditions and used the results to derive markers of chronic-inflammation and immune resolution.

Diversity in clinical outcomes following SARS-CoV-2 infection is attributed to heterogeneity in immune responses who, in turn, are influenced by individuals' age, ethnicity, sex and the presence of comorbidities [71]. Delayed and ineffective innate immunity leads to increased neutrophil recruitment in the blood, neutrophil infiltration into the lungs, changes in neutrophil phenotype, and/or formation of neutrophil extracellular traps [3,12,72–74], all of which have been associated with poor disease outcomes. To address the role of neutrophils of different phenotypes, we modeled two neutrophil subpopulations, activated $n(t)$ and apoptotic $a(t)$. Using the model, we examined the differences in total neutrophil levels at hospitalization $n_0 + a_0$, the estimated neutrophil activation rate α_c, and the estimated neutrophil apoptotosis rate ν when the model is fitted to immune population data from mild and severe clinical outcomes. We found higher values for all three markers with initial neutrophils having the biggest increase (2.3-times higher), compared to neutrophil activation (1.5-times higher), and phenotype change (1.3-times higher) in severe cases compared to mild cases. Data fitting indicated that the parameter space corresponding to severe disease outcomes is associated with the bistable kinetics of our model, while the parameter space corresponding to mild clinical outcome is associated with the monostable kinetics of our model (Figure 4). One dimensional bifurcation diagrams with respect to neutrophil recruitment rate α_c (Figure 5) and two-dimensional bifurcation diagrams with respect to α_c and initial activated neutrophils n_0 (Figure 7B) showed that lowering neutophil recruitment and/or the neutrophil activation can lead to immune resolution. One way to accomplish that is by understanding how comorbidities or pre-existing conditions affect neutrophil functionality, recruitment, are inherent dysregulation [75] as done in other diseases [12,76,77].

In our model, one way to control neutrophil activity is through recruitment of macrophages $m(t)$ which, in turn, enhance neutrophil apoptosis at rate ϕ. Data fitting showed decreased neutrophil apoptosis rates (12.4-times lower) in severe compared to mild cases. One dimensional bifurcation diagrams with respect to ϕ showed that increasing macrophage induced neutophil apoptosis can lead to immune resolution (Figure 6).

A common feature for severe COVID-19 clinical outcomes is the production of high levels of proinflammatory cytokines (such as IL-6), which in our model were generically combined under the cytokine population c. Paradoxically, IL-10, which is classified as an anti-inflammatory cytokine, is also elevated in severe cases [61]. To determine its role on overall immune dynamics, we considered an anti-inflammatory population $g(t)$ in our model, modeled its effect on neutrophil phenotype change and on lowering the recruitment of CD8 T-cells, and fitted it to IL-10 data. We found that the magnitude of anti-inflammatory population at hospital admission g_0 is 1.5-times higher in severe compared to mild cases. Using bifurcation analyses we investigated how changes in g_0 affect the results. We found that lowering g_0 allows for immune resolution for a larger n_0 parameter space (Figure 7A). This suggests that IL-10 fails to suppress the inflammation in COVID-19, a result seen in other inflammatory diseases [78,79].

An inefficient or delayed innate immune response to SARS-CoV-2 affects adaptive immune response priming, which can lead to long-term immune conditions and or fatalities [71]. In our model, we only consider the CD8 T-cell population $e(t)$, which is primed by antigen presenting cells (macrophages $m(t)$ in our case) and inhibited by anti-inflammatory mediators (IL-10 $g(t)$ in our case). We fitted the model to CD8 T-cell data from mild and severe cases, and found that the recruitment rate α_e is extremely low in the severe cases (six order of magnitude lower than in the mild cases). Using these results we calculated the neutrophil-to-CD8 T-cell ratio, which has been used in other studies as a severity marker [80–82]. We found that in mild cases N8R peak to $N8R = 13.1$, 3.25 days after hospital admission and decay to zero in the long-run. By contrast, in severe cases the N8R start at $N8R = 41$ at the time of hospital admission and settle at $N8R = 38$ in the long-run (Figure 4). Interestingly, we predict that these different results are heavily determined by the low recruitment rate of CD8 T-cells in severe cases, rather that differences in neutrophil levels between the two clinical outcomes.

Our study has several limitations. First, we do not explicitly model SARS-CoV-2 dynamics and instead model the inflammatory response following SARS-CoV-2-induced epithelial tissue damage. We use a functional response with oscillatory dynamics and fixed frequency, magnitude, and number of oscillations to model tissue damage (Figure 1). We investigated the dependence of the results on the changes in magnitude, frequency, and number of oscillations. We found that increased cycles of tissue damage result in prolonged inflammation, and higher tissue damage induces larger neutrophil recruitment in the short term, but neither of these factors affect long-term kinetics (Figure 8). More information is needed to determine whether this functional form is indicative of viral-induced tissue damage and early (before hospital admission) virus data would be necessary for a better description of virus-immune system feedback. Second, during data fitting, we made a number of adhoc assumptions that can affect our estimates. Moreover, the fits to limited data may lead to uncertainties in our estimates. To address that, we conducted semirelative sensitivity analyses (Appendix A), which showed that α_c and ν have strong effect on neutrophil, macrophage and proinflammatory populations and weak effect on the anti-inflammatory and CD8 T-cell populations (Figures A2 and A4) and ϕ and α_e have weak effect on all populations (Figures A1 and A3). Last, we considered a half-life of two weeks for macrophages [63]. Several studies have suggested a much longer half-life of 3 weeks–4 months [83,84], which may affect transient (but not long-term) dynamics.

6. Conclusions

In conclusion, we developed a mathematical model of neutrophil dynamics following infection and hospitalization with COVID-19. We fitted the model to the data and determined conditions needed for immune resolution.

Author Contributions: Conceptualization: Q.M.M. and S.M.C.; methodology, Q.M.M., S.M.C.; software, Q.M.M.; validation, Q.M.M., S.M.C.; formal analysis, Q.M.M., S.M.C.; investigation, Q.M.M., S.M.C.; resources, S.M.C.; writing—original draft preparation, Q.M.M., S.M.C.; writing—review and

editing, Q.M.M., S.M.C.; supervision, S.M.C.; funding acquisition, S.M.C. All authors have read and agreed to the published version of the manuscript.

Funding: S.M.C. and Q.M.M. were funded by National Science Foundation grants No. 1813011 and 2051820.

Institutional Review Board Statement: Not applicable.

Informed Consent Statement: Not applicable.

Data Availability Statement: Upon acceptance, data and code will be made available through GitHub.

Acknowledgments: S.M.C. and Q.M.M. acknowledge salary support from National Science Foundation grants No. 1813011 and 2051820.

Conflicts of Interest: The authors declare no conflict of interest.

Appendix A

We conduct a formal sensitivity analysis on the system of equations given in Equation (3). We let $\left\{n_\phi, a_\phi, m_\phi, c_\phi, g_\phi, e_\phi\right\} = \left\{\frac{\partial n}{\partial \phi}, \frac{\partial a}{\partial \phi}, \frac{\partial m}{\partial \phi}, \frac{\partial c}{\partial \phi}, \frac{\partial g}{\partial \phi}, \frac{\partial e}{\partial \phi}\right\}$ be the sensitivity curves with respect to ϕ. The corresponding sensitivity equations with respect to parameter ϕ are

$$\begin{aligned}
\frac{dn_\phi(t,\phi)}{dt} &= \alpha_c c_\phi - \nu\left(g n_\phi + n g_\phi\right),\\
\frac{da_\phi(t,\phi)}{dt} &= \nu\left(g n_\phi + n g_\phi\right) - \gamma_a a_\phi - \phi m a_\phi - \phi a m_\phi - m a,\\
\frac{dm_\phi(t,\phi)}{dt} &= \alpha_m c_\phi - \gamma_m m_\phi,\\
\frac{dc_\phi(t,\phi)}{dt} &= 2 a a_\phi \frac{\gamma_a k_a \beta_a^2}{(\beta_a^2 + a^2)^2} - \gamma_c c_\phi,\\
\frac{dg_\phi(t,\phi)}{dt} &= k_g\left(\phi m a_\phi + \phi a m_\phi + m a\right) - \gamma_g g_\phi,\\
\frac{de_\phi(t,\phi)}{dt} &= -\alpha_e \frac{\beta_e m g_\phi}{(1+\beta_e g)^2} + \alpha_e \frac{m_\phi}{(1+\beta_e g)} - \gamma_e e_\phi
\end{aligned} \tag{A1}$$

Using the parameters in Tables 1 and 2 (severe case) we plotted the semirelative curves given by $(\phi n_\phi, \phi a_\phi, \phi m_\phi, \phi c_\phi, \phi g_\phi, \phi g_\phi)$ which showed low effect of ϕ on all populations (see Figure A1).

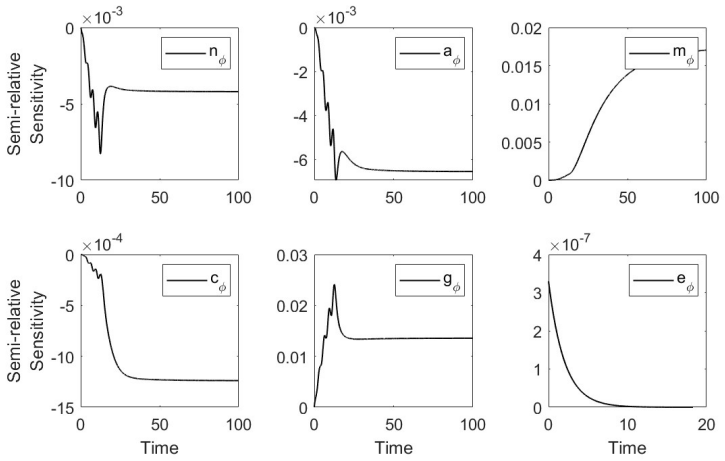

Figure A1. Semi-relative sensitivity curves with respect to ϕ.

We let $\left\{n_{\alpha_c}, a_{\alpha_c}, m_{\alpha_c}, c_{\alpha_c}, g_{\alpha_c}, e_{\alpha_c}\right\} = \left\{\frac{\partial n}{\partial \alpha_c}, \frac{\partial a}{\partial \alpha_c}, \frac{\partial m}{\partial \alpha_c}, \frac{\partial c}{\partial \alpha_c}, \frac{\partial g}{\alpha_c}, \frac{\partial e}{\partial \alpha_c}\right\}$ be the sensitivity curves with respect to α_c. The corresponding sensitivity equations with respect to the parameter α_c are

$$\begin{aligned}
\frac{dn_{\alpha_c}(t,\alpha_c)}{dt} &= \alpha_c c_{\alpha_c} + c - \nu(g n_{\alpha_c} + n g_{\alpha_c}),\\
\frac{da_{\alpha_c}(t,\alpha_c)}{dt} &= \nu(g n_{\alpha_c} + n g_{\alpha_c}) - \gamma_a a_{\alpha_c} - \phi(m a_{\alpha_c} + a m_{\alpha_c}),\\
\frac{dm_{\alpha_c}(t,\alpha_c)}{dt} &= \alpha_m c_{\alpha_c} - \gamma_m m_{\alpha_c},\\
\frac{dc_{\alpha_c}(t,\alpha_c)}{dt} &= 2a a_{\alpha_c} \frac{\gamma_a k_a \beta_a^2}{(\beta_a^2 + a^2)^2} - \gamma_c c_{\alpha_c},\\
\frac{dg_{\alpha_c}(t,\alpha_c)}{dt} &= k_g \phi(m a_{\alpha_c} + a m_{\alpha_c}) - \gamma_g g_{\alpha_c},\\
\frac{de_{\alpha_c}(t,\alpha_c)}{dt} &= -\alpha_e \frac{\beta_e m g_{\alpha_c}}{(1+\beta_e g)^2} + \alpha_e \frac{m_{\alpha_c}}{(1+\beta_e g)} - \gamma_e e_{\alpha_c}.
\end{aligned} \tag{A2}$$

Using the parameters in Tables 1 and 2 (severe case) we plotted the semirelative curves given by $(\alpha_c n_{\alpha_c}, \alpha_c a_{\alpha_c}, \alpha_c m_{\alpha_c}, \alpha_c c_{\alpha_c}, \alpha_c g_{\alpha_c}, \alpha_c g_{\alpha_c})$ which showed large effect of α_c on the neutrophil, macrophage and proinflammatory populations and weak effect on anti-inflammatory and CD8 T-cell populations (see Figure A2).

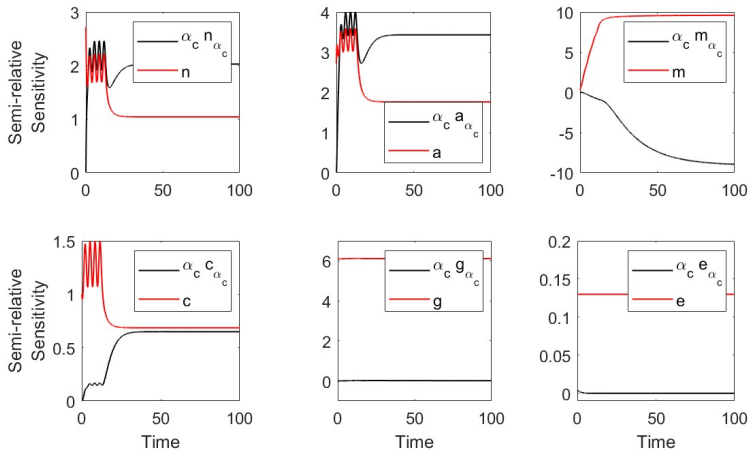

Figure A2. Semirelative sensitivity curves with respect to α_c.

We let $\left\{n_{\alpha_e}, a_{\alpha_e}, m_{\alpha_e}, c_{\alpha_e}, g_{\alpha_e}, e_{\alpha_e}\right\} = \left\{\frac{\partial n}{\partial \alpha_e}, \frac{\partial a}{\partial \alpha_e}, \frac{\partial m}{\partial \alpha_e}, \frac{\partial c}{\partial \alpha_e}, \frac{\partial g}{\alpha_e}, \frac{\partial e}{\partial \alpha_e}\right\}$ be the sensitivity curves with respect to α_e. The corresponding sensitivity equations with respect to the parameter α_e are

$$\begin{aligned}
\frac{dn_{\alpha_e}(t,\alpha_e)}{dt} &= \alpha_c c_{\alpha_e} - \nu(gn_{\alpha_e} + ng_{\alpha_e}),\\
\frac{da_{\alpha_e}(t,\alpha_e)}{dt} &= \nu(gn_{\alpha_e} + ng_{\alpha_e}) - \gamma_a a_{\alpha_e} - \phi(ma_{\alpha_e} + am_{\alpha_e}),\\
\frac{dm_{\alpha_e}(t,\alpha_e)}{dt} &= \alpha_m c_{\alpha_e} - \gamma_m m_{\alpha_e},\\
\frac{dc_{\alpha_e}(t,\alpha_e)}{dt} &= 2aa_{\alpha_e}\frac{\gamma_a k_a \beta_a^2}{(\beta_a^2 + a^2)^2} - \gamma_c c_{\alpha_e},\\
\frac{dg_{\alpha_e}(t,\alpha_e)}{dt} &= k_g\phi(ma_{\alpha_e} + am_{\alpha_e}) - \gamma_g g_{\alpha_e},\\
\frac{de_{\alpha_e}(t,\alpha_e)}{dt} &= -\alpha_e\frac{\beta_e m g_{\alpha_e}}{(1+\beta_e g)^2} + \frac{\alpha_e m_{\alpha_e} + m}{(1+\beta_e g)} - \gamma_e e_{\alpha_e}.
\end{aligned} \tag{A3}$$

Using the parameters in Tables 1 and 2 (severe case), we plotted the semirelative curves given by $(\alpha_e n_{\alpha_e}, \alpha_e a_{\alpha_e}, \alpha_e m_{\alpha_e}, \alpha_e c_{\alpha_e}, \alpha_e g_{\alpha_e}, \alpha_e g_{\alpha_e})$ which showed low effect of α_e on all populations (see Figure A3).

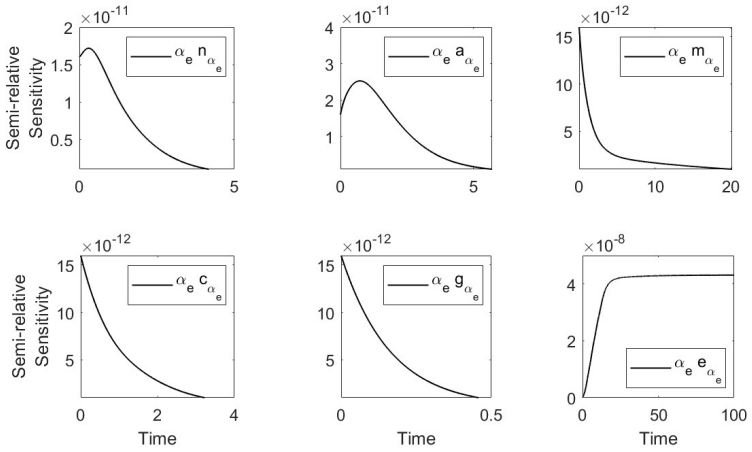

Figure A3. Semi-relative sensitivity curves with respect to α_e.

We let $\left\{n_\nu, a_\nu, m_\nu, c_\nu, g_\nu, e_\nu\right\} = \left\{\frac{\partial n}{\partial \nu}, \frac{\partial a}{\partial \nu}, \frac{\partial m}{\partial \nu}, \frac{\partial c}{\partial \nu}, \frac{\partial g}{\nu}, \frac{\partial e}{\partial \nu}\right\}$ be the sensitivity curves with respect to ν. The corresponding sensitivity equations with respect to the parameter ν are

$$\begin{aligned}
\frac{dn_\nu(t,\nu)}{dt} &= \alpha_c c_\nu - \nu g n_\nu - \nu n g_\nu - ng,\\
\frac{da_\nu(t,\nu)}{dt} &= \nu g n_\nu + \nu n g_\nu + ng - \gamma_a a_\nu - \phi(ma_\nu + am_\nu),\\
\frac{dm_\nu(t,\nu)}{dt} &= \alpha_m c_\nu - \gamma_m m_\nu,\\
\frac{dc_\nu(t,\nu)}{dt} &= 2aa_\nu\frac{\gamma_a k_a \beta_a^2}{(\beta_a^2 + a^2)^2} - \gamma_c c_\nu\\
\frac{dg_\nu(t,\nu)}{dt} &= k_g\phi(ma_\nu + am_\nu) - \gamma_g g_\nu,\\
\frac{de_\nu(t,\nu)}{dt} &= -\alpha_e\frac{\beta_e m g_\nu}{(1+\beta_e g)^2} + \alpha_e\frac{m_\nu}{(1+\beta_e g)} - \gamma_e e_\nu
\end{aligned} \tag{A4}$$

Using the parameters in Tables 1 and 2 (severe case), we plotted the semirelative curves given by $(\nu n_\nu, \nu a_\nu, \nu m_\nu, \nu c_\nu, \nu g_\nu, \nu g_\nu)$ which showed large effect of ν on the neutrophil, macrophage, and proinflammatory populations and weak effect on anti-inflammatory and CD8 T-cell populations (see Figure A4).

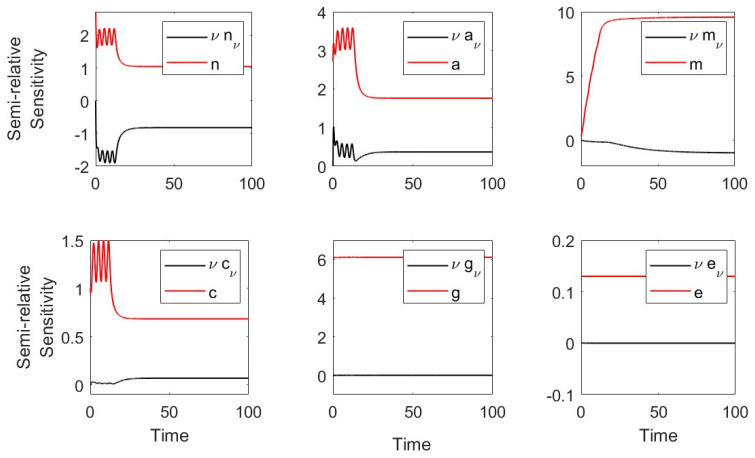

Figure A4. Semirelative sensitivity curves with respect to ν.

References

1. Borczuk, A.C.; Yantiss, R.K. The pathogenesis of coronavirus-19 disease. *J. Biomed. Sci.* **2022**, *29*, 1–15. [CrossRef] [PubMed]
2. Soy, M.; Keser, G.; Atagündüz, P.; Tabak, F.; Atagu anduz, I.; Kayhan, S. Cytokine storm in COVID-19: Pathogenesis and overview of anti-inflammatory agents used in treatment. *Clin. Rheumatol.* **2020**, *39*, 2085–2094. [CrossRef]
3. Wilk, A.J.; Lee, M.J.; Wei, B.; Parks, B.; Pi, R.; Martinez-Colon, G.J.; Ranganath, T.; Zhao, N.Q.; Taylor, S.; Becker, W.; et al. Multi-omic profiling reveals widespread dysregulation of innate immunity and hematopoiesis in COVID-19. *J. Exp. Med.* **2021**, *218*, e20210582. [CrossRef]
4. Dorgham, K.; Quentric, P.; Gökkaya, M.; Marot, S.; Parizot, C.; Sauce, D.; Guihot, A.; Luyt, C.E.; Schmidt, M.; Mayaux, J.; et al. Distinct cytokine profiles associated with COVID-19 severity and mortality. *J. Allergy Clin. Immunol.* **2021**, *147*, 2098–2107. [CrossRef]
5. Montazersaheb, S.; Hosseiniyan Khatibi, S.M.; Hejazi, M.S.; Tarhriz, V.; Farjami, A.; Ghasemian Sorbeni, F.; Farahzadi, R.; Ghasemnejad, T. COVID-19 infection: An overview on cytokine storm and related interventions. *Virol. J.* **2022**, *19*, 1–15. [CrossRef]
6. Hu, B.; Huang, S.; Yin, L. The cytokine storm and COVID-19. *J. Med. Virol.* **2021**, *93*, 250–256. [CrossRef] [PubMed]
7. de Kleijn, S.; Langereis, J.D.; Leentjens, J.; Kox, M.; Netea, M.G.; Koenderman, L.; Ferwerda, G.; Pickkers, P.; Hermans, P.W. IFN-γ-stimulated neutrophils suppress lymphocyte proliferation through expression of PD-L1. *PLoS ONE* **2013**, *8*, e72249. [CrossRef] [PubMed]
8. Juss, J.K.; House, D.; Amour, A.; Begg, M.; Herre, J.; Storisteanu, D.M.; Hoenderdos, K.; Bradley, G.; Lennon, M.; Summers, C.; et al. Acute respiratory distress syndrome neutrophils have a distinct phenotype and are resistant to phosphoinositide 3-kinase inhibition. *Am. J. Respir. Crit. Care Med.* **2016**, *194*, 961–973. [CrossRef]
9. Nathan, C.; Ding, A. Nonresolving inflammation. *Cell* **2010**, *140*, 871–882. [CrossRef] [PubMed]
10. Minucci, S.B.; Heise, R.L.; Reynolds, A.M. Review of mathematical modeling of the inflammatory response in lung infections and injuries. *Front. Appl. Math. Stat.* **2020**, *6*, 36. [CrossRef]
11. Lawrence, T.; Gilroy, D.W. Chronic inflammation: A failure of resolution? *Int. J. Exp. Pathol.* **2007**, *88*, 85–94. [CrossRef] [PubMed]
12. Reusch, N.; de Domenico, E.; Bonaguro, L.; Schulte-Schrepping, J.; Baßler, K.; Schultze, J.L.; Aschenbrenner, A.C. Neutrophils in COVID-19. *Front. Immunol.* **2021**, *12*, 952. [CrossRef]
13. Liu, J.; Li, S.; Liu, J.; Liang, B.; Wang, X.; Wang, H.; Li, W.; Tong, Q.; Yi, J.; Zhao, L.; et al. Longitudinal characteristics of lymphocyte responses and cytokine profiles in the peripheral blood of SARS-CoV-2 infected patients. *eBioMedicine* **2020**, *55*, 102763. [CrossRef]
14. Wang, D.; Hu, B.; Hu, C.; Zhu, F.; Liu, X.; Zhang, J.; Wang, B.; Xiang, H.; Cheng, Z.; Xiong, Y.; et al. Clinical characteristics of 138 hospitalized patients with 2019 novel coronavirus–infected pneumonia in Wuhan, China. *JAMA* **2020**, *323*, 1061–1069. [CrossRef] [PubMed]
15. Huang, W.; Li, M.; Luo, G.; Wu, X.; Su, B.; Zhao, L.; Zhang, S.; Chen, X.; Jia, M.; Zhu, J.; et al. The inflammatory factors associated with disease severity to predict COVID-19 progression. *J. Immunol.* **2021**, *206*, 1597–1608. [CrossRef] [PubMed]
16. Guan, J.; Wei, X.; Qin, S.; Liu, X.; Jiang, Y.; Chen, Y.; Chen, Y.; Lu, H.; Qian, J.; Wang, Z.; et al. Continuous tracking of COVID-19 patients' immune status. *Int. Immunopharmacol.* **2020**, *89*, 107034. [CrossRef] [PubMed]
17. Zhang, H.; Wang, X.; Fu, Z.; Luo, M.; Zhang, Z.; Zhang, K.; He, Y.; Wan, D.; Zhang, L.; Wang, J.; et al. Potential factors for prediction of disease severity of COVID-19 patients. *medRxiv* **2020**. [CrossRef]
18. Kuppalli, K.; Rasmussen, A.L. A glimpse into the eye of the COVID-19 cytokine storm. *eBioMedicine* **2020**, *55*, 102789. [CrossRef]
19. Vaughan, L.E.; Ranganathan, P.R.; Kumar, R.G.; Wagner, A.K.; Rubin, J.E. A mathematical model of neuroinflammation in severe clinical traumatic brain injury. *J. Neuroinflamm.* **2018**, *15*, 1–19. [CrossRef]

20. Yang, Q.; Berthiaume, F.; Androulakis, I.P. A quantitative model of thermal injury-induced acute inflammation. *Math. Biosci.* **2011**, *229*, 135–148. [CrossRef]
21. Minucci, S.; Heise, R.L.; Valentine, M.S.; Gninzeko, F.J.K.; Reynolds, A.M. Mathematical modeling of ventilator-induced lung inflammation. *J. Theor. Biol.* **2021**, *526*, 110738. [CrossRef]
22. Kogan, Y.; Agur, Z.; Elishmereni, M. A mathematical model for the immunotherapeutic control of the Th1/Th2 imbalance in melanoma. *Discret. Contin. Dyn. Syst. B* **2013**, *18*, 1017–1030. [CrossRef]
23. Andersen, M.; Sajid, Z.; Pedersen, R.K.; Gudmand-Hoeyer, J.; Ellervik, C.; Skov, V.; Kjær, L.; Pallisgaard, N.; Kruse, T.A.; Thomassen, M.; et al. Mathematical modelling as a proof of concept for MPNs as a human inflammation model for cancer development. *PLoS ONE* **2017**, *12*, e0183620. [CrossRef]
24. Baker, M.; Denman-Johnson, S.; Brook, B.S.; Gaywood, I.; Owen, M.R. Mathematical modelling of cytokine-mediated inflammation in rheumatoid arthritis. *Math. Med. Biol. J. IMA* **2013**, *30*, 311–337. [CrossRef]
25. Moise, N.; Friedman, A. Rheumatoid arthritis-a mathematical model. *J. Theor. Biol.* **2019**, *461*, 17–33. [CrossRef] [PubMed]
26. El Khatib, N.; Génieys, S.; Kazmierczak, B.; Volpert, V. Mathematical modelling of atherosclerosis as an inflammatory disease. *Philos. Trans. R. Soc. A Math. Phys. Eng. Sci.* **2009**, *367*, 4877–4886. [CrossRef] [PubMed]
27. Leber, A.; Abedi, V.; Hontecillas, R.; Viladomiu, M.; Hoops, S.; Ciupe, S.; Caughman, J.; Andrew, T.; Bassaganya-Riera, J. Bistability analyses of CD4+ T follicular helper and regulatory cells during Helicobacter pylori infection. *J. Theor. Biol.* **2016**, *398*, 74–84. [CrossRef] [PubMed]
28. Nelson, P.; Smith, N.; Ciupe, S.; Zou, W.; Omenn, G.S.; Pietropaolo, M. Modeling dynamic fluctuations in type 1 diabetes progression: Quantifying β-cell variation after the appearance of islet-specific autoimmune responses. *Math. Biosci. Eng. MBE* **2009**, *6*, 753–778.
29. Caudill, L.; Lynch, F. A mathematical model of the inflammatory response to pathogen challenge. *Bull. Math. Biol.* **2018**, *80*, 2242–2271. [CrossRef]
30. Dunster, J.L.; Byrne, H.M.; King, J.R. The resolution of inflammation: A mathematical model of neutrophil and macrophage interactions. *Bull. Math. Biol.* **2014**, *76*, 1953–1980. [CrossRef]
31. Ciupe, S.M.; Boribong, B.P.; Kadelka, S.; Jones, C.N. Bistable Mathematical Model of Neutrophil Migratory Patterns After LPS-Induced Epigenetic Reprogramming. *Front. Genet.* **2021**, *12*, 633963. [CrossRef]
32. Reynolds, A.; Rubin, J.; Clermont, G.; Day, J.; Vodovotz, Y.; Ermentrout, G.B. A reduced mathematical model of the acute inflammatory response: I. Derivation of model and analysis of anti-inflammation. *J. Theor. Biol.* **2006**, *242*, 220–236. [CrossRef] [PubMed]
33. Clermont, G.; Chow, C.C.; Constantine, G.M.; Vodovotz, Y.; Bartels, J. Mathematical and statistical modeling of acute inflammation. In *Classification, Clustering, and Data Mining Applications*; Springer: Cham, Switzerland, 2004; pp. 457–467.
34. Mathew, S.; Bartels, J.; Banerjee, I.; Vodovotz, Y. Global sensitivity analysis of a mathematical model of acute inflammation identifies nonlinear dependence of cumulative tissue damage on host interleukin-6 responses. *J. Theor. Biol.* **2014**, *358*, 132–148. [CrossRef]
35. Kadelka, S.; Boribong, B.P.; Li, L.; Ciupe, S.M. Modeling the bistable dynamics of the innate immune system. *Bull. Math. Biol.* **2019**, *81*, 256–276. [CrossRef]
36. Beauchemin, C.A.; Handel, A. A review of mathematical models of influenza A infections within a host or cell culture: Lessons learned and challenges ahead. *BMC Public Health* **2011**, *11*, S7. [CrossRef]
37. Doherty, P.C.; Turner, S.J.; Webby, R.G.; Thomas, P.G. Influenza and the challenge for immunology. *Nat. Immunol.* **2006**, *7*, 449–455. [CrossRef] [PubMed]
38. Thomas, P.G.; Keating, R.; Hulse-Post, D.J.; Doherty, P.C. Cell-mediated protection in influenza infection. *Emerg. Infect. Dis.* **2006**, *12*, 48–54. [CrossRef]
39. Maines, T.R.; Szretter, K.J.; Perrone, L.; Belser, J.A.; Bright, R.A.; Zeng, H.; Tumpey, T.M.; Katz, J.M. Pathogenesis of emerging avian influenza viruses in mammals and the host innate immune response. *Immunol. Rev.* **2008**, *225*, 68–84. [CrossRef]
40. Miao, H.; Hollenbaugh, J.A.; Zand, M.S.; Holden-Wiltse, J.; Mosmann, T.R.; Perelson, A.S.; Wu, H.; Topham, D.J. Quantifying the early immune response and adaptive immune response kinetics in mice infected with influenza A virus. *J. Virol.* **2010**, *84*, 6687–6698. [CrossRef] [PubMed]
41. Ciupe, S.M.; Ribeiro, R.M.; Perelson, A.S. Antibody responses during hepatitis B viral infection. *PLoS Comput. Biol.* **2014**, *10*, e1003730. [CrossRef] [PubMed]
42. Ciupe, S.M.; Vaidya, N.K.; Forde, J.E. Early events in hepatitis B infection: The role of inoculum dose. *Proc. R. Soc. B* **2021**, *288*, 20202715. [CrossRef] [PubMed]
43. Ciupe, S.M.; Hews, S. Mathematical models of e-antigen mediated immune tolerance and activation following prenatal HBV infection. *PLoS ONE* **2012**, *7*, e39591. [CrossRef] [PubMed]
44. Ciupe, S.M.; Ribeiro, R.M.; Nelson, P.W.; Dusheiko, G.; Perelson, A.S. The role of cells refractory to productive infection in acute hepatitis B viral dynamics. *Proc. Natl. Acad. Sci. USA* **2007**, *104*, 5050–5055. [CrossRef]
45. Gralinski, L.E.; Bankhead, A., III; Jeng, S.; Menachery, V.D.; Proll, S.; Belisle, S.E.; Matzke, M.; Webb-Robertson, B.J.M.; Luna, M.L.; Shukla, A.K.; et al. Mechanisms of severe acute respiratory syndrome coronavirus-induced acute lung injury. *mBio* **2013**, *4*, e00271-13. [CrossRef] [PubMed]

46. Guillon, P.; Clément, M.; Sébille, V.; Rivain, J.G.; Chou, C.F.; Ruvoën-Clouet, N.; le Pendu, J. Inhibition of the interaction between the SARS-CoV spike protein and its cellular receptor by anti-histo-blood group antibodies. *Glycobiology* **2008**, *18*, 1085–1093. [CrossRef]
47. Jenner, A.L.; Aogo, R.A.; Alfonso, S.; Crowe, V.; Smith, A.P.; Morel, P.A.; Davis, C.L.; Smith, A.M.; Craig, M. COVID-19 virtual patient cohort reveals immune mechanisms driving disease outcomes. *PLoS Pathog.* **2021**, *17*, e1009753. [CrossRef]
48. Du, S.Q.; Yuan, W. Mathematical modeling of interaction between innate and adaptive immune responses in COVID-19 and implications for viral pathogenesis. *J. Med. Virol.* **2020**, *92*, 1615–1628. [CrossRef]
49. Hernandez-Vargas, E.A.; Velasco-Hernandez, J.X. In-host mathematical modelling of COVID-19 in humans. *Annu. Rev. Control.* **2020**, *50*, 448–456. [CrossRef]
50. Chimal-Eguia, J.C. Mathematical model of antiviral immune response against the COVID-19 virus. *Mathematics* **2021**, *9*, 1356. [CrossRef]
51. Sahoo, S.; Jhunjhunwala, S.; Jolly, M.K. The good, the bad and the ugly: A mathematical model investigates the differing outcomes among COVID-19 patients. *J. Indian Inst. Sci.* **2020**, *100*, 673–681. [CrossRef]
52. Ghosh, I. Within host dynamics of SARS-CoV-2 in humans: Modeling immune responses and antiviral treatments. *SN Comput. Sci.* **2021**, *2*, 1–12. [CrossRef] [PubMed]
53. Heitzman-Breen, N.; Ciupe, S.M. Modeling within-host and aerosol dynamics of SARS-CoV-2: The relationship with infectiousness. *PLoS Comput. Biol.* **2022**, *18*, e1009997. [CrossRef]
54. Ke, R.; Zitzmann, C.; Ho, D.D.; Ribeiro, R.M.; Perelson, A.S. In vivo kinetics of SARS-CoV-2 infection and its relationship with a person's infectiousness. *Proc. Natl. Acad. Sci. USA* **2021**, *118*, e2111477118. [CrossRef] [PubMed]
55. Ciupe, S.M.; Tuncer, N. Identifiability of parameters in mathematical models of SARS-CoV-2 infections in humans. *Sci. Rep.* **2022**, *12*, 14637. [CrossRef] [PubMed]
56. Wang, X.; Wang, S.; Wang, J.; Rong, L. A Multiscale Model of COVID-19 Dynamics. *Bull. Math. Biol.* **2022**, *84*, 99. [CrossRef] [PubMed]
57. Schwarze, J.; Mackenzie, K.J. Novel insights into immune and inflammatory responses to respiratory viruses. *Thorax* **2013**, *68*, 108–110. [CrossRef] [PubMed]
58. Sugimoto, M.A.; Sousa, L.P.; Pinho, V.; Perretti, M.; Teixeira, M.M. Resolution of inflammation: What controls its onset? *Front. Immunol.* **2016**, *7*, 160. [CrossRef] [PubMed]
59. Eming, S.A.; Martin, P.; Tomic-Canic, M. Wound repair and regeneration: Mechanisms, signaling, and translation. *Sci. Transl. Med.* **2014**, *6*, 265sr6. [CrossRef]
60. Serhan, C.N.; Savill, J. Resolution of inflammation: The beginning programs the end. *Nat. Immunol.* **2005**, *6*, 1191–1197. [CrossRef]
61. Liu, Y.; Yang, Y.; Zhang, C.; Huang, F.; Wang, F.; Yuan, J.; Wang, Z.; Li, J.; Li, J.; Feng, C.; et al. Clinical and biochemical indexes from 2019-nCoV infected patients linked to viral loads and lung injury. *Sci. China Life Sci.* **2020**, *63*, 364–374. [CrossRef]
62. Henson, P.M. Dampening inflammation. *Nat. Immunol.* **2005**, *6*, 1179–1181. [CrossRef] [PubMed]
63. Godleski, J.J.; Brain, J.D. The origin of alveolar macrophages in mouse radiation chimeras. *J. Exp. Med.* **1972**, *136*, 630–643. [CrossRef] [PubMed]
64. McDonagh, M.; Bell, E. The survival and turnover of mature and immature CD8 T cells. *Immunology* **1995**, *84*, 514–520.
65. Ahmed, R.; Gray, D. Immunological memory and protective immunity: Understanding their relation. *Science* **1996**, *272*, 54–60. [CrossRef]
66. Ciupe, S.M.; Ribeiro, R.M.; Nelson, P.W.; Perelson, A.S. Modeling the mechanisms of acute hepatitis B virus infection. *J. Theor. Biol.* **2007**, *247*, 23–35. [CrossRef] [PubMed]
67. Fedorak, R.N.; Gangl, A.; Elson, C.O.; Rutgeerts, P.; Schreiber, S.; Wild, G.; Hanauer, S.B.; Kilian, A.; Cohard, M.; LeBeaut, A.; et al. Recombinant human interleukin 10 in the treatment of patients with mild to moderately active Crohn's disease. *Gastroenterology* **2000**, *119*, 1473–1482. [CrossRef]
68. Aziz, N.; Detels, R.; Quint, J.J.; Li, Q.; Gjertson, D.; Butch, A.W. Stability of cytokines, chemokines and soluble activation markers in unprocessed blood stored under different conditions. *Cytokine* **2016**, *84*, 17–24. [CrossRef]
69. Kuribayashi, T. Elimination half-lives of interleukin-6 and cytokine-induced neutrophil chemoattractant-1 synthesized in response to inflammatory stimulation in rats. *Lab. Anim. Res.* **2018**, *34*, 80–83. [CrossRef]
70. Huhn, R.D.; Radwanski, E.; Gallo, J.; Affrime, M.B.; Sabo, R.; Gonyo, G.; Monge, A.; Cutler, D.L. Pharmacodynamics of subcutaneous recombinant human interleukin-10 in healthy volunteers. *Clin. Pharmacol. Ther.* **1997**, *62*, 171–180. [CrossRef]
71. Sette, A.; Crotty, S. Adaptive immunity to SARS-CoV-2 and COVID-19. *Cell* **2021**, *184*, 861–880. [CrossRef] [PubMed]
72. Del Valle, D.M.; Kim-Schulze, S.; Huang, H.H.; Beckmann, N.D.; Nirenberg, S.; Wang, B.; Lavin, Y.; Swartz, T.H.; Madduri, D.; Stock, A.; et al. An inflammatory cytokine signature predicts COVID-19 severity and survival. *Nat. Med.* **2020**, *26*, 1636–1643. [CrossRef] [PubMed]
73. Radermecker, C.; Detrembleur, N.; Guiot, J.; Cavalier, E.; Henket, M.; d'Emal, C.; Vanwinge, C.; Cataldo, D.; Oury, C.; Delvenne, P.; et al. Neutrophil extracellular traps infiltrate the lung airway, interstitial, and vascular compartments in severe COVID-19. *J. Exp. Med.* **2020**, *217*, e20201012. [CrossRef] [PubMed]
74. McKenna, E.; Wubben, R.; Isaza-Correa, J.M.; Melo, A.M.; Mhaonaigh, A.U.; Conlon, N.; O'Donnell, J.S.; Ní Cheallaigh, C.; Hurley, T.; Stevenson, N.J.; et al. Neutrophils in COVID-19: Not Innocent Bystanders. *Front. Immunol.* **2022**, *13*, 2548. [CrossRef]

75. Bigdelou, B.; Sepand, M.R.; Najafikhoshnoo, S.; Negrete, J.A.T.; Sharaf, M.; Ho, J.Q.; Sullivan, I.; Chauhan, P.; Etter, M.; Shekarian, T.; et al. COVID-19 and Preexisting Comorbidities: Risks, Synergies, and Clinical Outcomes. *Front. Immunol.* **2022**, *13*, 2077. [CrossRef] [PubMed]
76. Rennard, S.I.; Dale, D.C.; Donohue, J.F.; Kanniess, F.; Magnussen, H.; Sutherland, E.R.; Watz, H.; Lu, S.; Stryszak, P.; Rosenberg, E.; et al. CXCR2 antagonist MK-7123. A phase 2 proof-of-concept trial for chronic obstructive pulmonary disease. *Am. J. Respir. Crit. Care Med.* **2015**, *191*, 1001–1011. [CrossRef] [PubMed]
77. Stockley, R.; de Soyza, A.; Gunawardena, K.; Perrett, J.; Forsman-Semb, K.; Entwistle, N.; Snell, N. Phase II study of a neutrophil elastase inhibitor (AZD9668) in patients with bronchiectasis. *Respir. Med.* **2013**, *107*, 524–533. [CrossRef]
78. Antoniv, T.T.; Ivashkiv, L.B. Dysregulation of interleukin-10–dependent gene expression in rheumatoid arthritis synovial macrophages. *Arthritis Rheum.* **2006**, *54*, 2711–2721. [CrossRef]
79. Ji, J.D.; Tassiulas, I.; Park-Min, K.H.; Aydin, A.; Mecklenbrauker, I.; Tarakhovsky, A.; Pricop, L.; Salmon, J.E.; Ivashkiv, L.B. Inhibition of interleukin 10 signaling after Fc receptor ligation and during rheumatoid arthritis. *J. Exp. Med.* **2003**, *197*, 1573–1583. [CrossRef]
80. Xue, T.C.; Zhang, L.; Xie, X.Y.; Ge, N.L.; Li, L.X.; Zhang, B.H.; Ye, S.L.; Ren, Z.G. Prognostic significance of the neutrophil-to-lymphocyte ratio in primary liver cancer: A meta-analysis. *PLoS ONE* **2014**, *9*, e96072. [CrossRef]
81. Carus, A.; Ladekarl, M.; Hager, H.; Nedergaard, B.; Donskov, F. Tumour-associated CD66b+ neutrophil count is an independent prognostic factor for recurrence in localised cervical cancer. *Br. J. Cancer* **2013**, *108*, 2116–2122. [CrossRef]
82. Hufford, M.M.; Richardson, G.; Zhou, H.; Manicassamy, B.; García-Sastre, A.; Enelow, R.I.; Braciale, T.J. Influenza-infected neutrophils within the infected lungs act as antigen presenting cells for anti-viral CD8+ T cells. *PLoS ONE* **2012**, *7*, e46581. [CrossRef]
83. Murphy, J.; Summer, R.; Wilson, A.A.; Kotton, D.N.; Fine, A. The prolonged life-span of alveolar macrophages. *Am. J. Respir. Cell Mol. Biol.* **2008**, *38*, 380–385. [CrossRef] [PubMed]
84. Ufimtseva, E.; Eremeeva, N.; Petrunina, E.; Umpeleva, T.; Karskanova, S.; Bayborodin, S.; Vakhrusheva, D.; Kravchenko, M.; Skornyakov, S. Ex vivo expansion of alveolar macrophages with Mycobacterium tuberculosis from the resected lungs of patients with pulmonary tuberculosis. *PLoS ONE* **2018**, *13*, e0191918. [CrossRef] [PubMed]